Linköping Studies in Science and Technology
Licentiate Thesis No. 1542

Growth and Characterization of Amorphous TiAlSiN and HfAlSiN Thin Films

Hanna Fager

Linköpings universitet
INSTITUTE OF TECHNOLOGY

LIU-TEK-LIC-2012:27
Thin Film Physics Division
Department of Physics, Chemistry, and Biology (IFM)
Linköping University, SE-581 83 Linköping, Sweden

Linköping 2012

ISBN 978-91-7519-843-9
ISSN 0280-7971

Printed by LiU-Tryck 2012

Abstract

This Thesis explores amorphous transition metal nitrides for cutting tool applications. The aim is to extend the knowledge on amorphous nitride thin films, to describe the growth process, and to explore ways of characterizing these novel complex materials.

Thin films of Ti-Al-Si-N and Hf-Al-Si-N were fabricated using industrial cathodic arc evaporation and magnetically-unbalanced reactive magnetron sputtering, respectively. The microstructure of the films was studied using x-ray diffraction (XRD) and transmission electron microscopy (TEM), while compositional analysis of the films was performed by spectroscopic techniques (EDS, SIMS, and RBS). The mechanical properties were investigated by nanoindentation.

The Ti-Al-Si-N films were grown on cemented carbide substrates using Ti-Al-Si compound cathodes in an N_2 atmosphere. High Al and Si concentrations in the films (i.e., 12 at% Si and 18 at% Al) promote renucleation and result in x-ray amorphous films. High resolution TEM (HRTEM) reveals isolated grains, $\sim$ 2 nm in size, embedded in an amorphous matrix. Annealing experiments show that the films are thermally stable up to 900 °C. They exhibit age hardening, with an increase in hardness from 21.9 GPa for as-deposited films to 31.6 GPa at 1000 °C. At 1100 °C severe out-diffusion of Co and W from the substrate occurs, and the films recrystallize into c-TiN and w-AlN.

The single layer Hf-Al-Si-N and multilayer Hf-Al-Si-N/HfN films were grown on Si(001) substrates from a single $Hf_{0.60}Al_{0.20}Si_{0.20}$ alloy target in an N_2/Ar atmosphere. The composition and nanostructure of the films was controlled during growth by independently varying the ion energy (E_i) and the ion-to-metal flux ratio (J_i/J_{Me}). With J_i/J_{Me}=8, the nanostructure and composition of the films changes from x-ray amorphous with a Hf content of 0.6, to an amorphous matrix with encapsulated nanocrystals with 0.66≤Hf≤0.84, to nanocrystalline with 0.96≤Hf≤1.00, when increasing E_i from 15 to 65 eV. Varying J_i/J_{Me} with E_i=13 eV yields electron-diffraction amorphous films at substrate temperatures of 100 °C. Hf-Al-Si-N/HfN multilayers with periods Λ=2-20 nm exhibit enhanced fracture toughness compared to polycrystalline VN, TiN, and $Ti_{0.5}Al_{0.5}N$ reference samples; multilayer hardness values increase from 20 GPa with Λ=20 nm to 27 GPa with Λ=2 nm.

Preface

This is a report of my research work from November 2009 to July 2012. During this time, the main focus has been to study growth and to characterize amorphous Ti-Al-Si-N and Hf-Al-Si-N thin films with competing crystallization and nanostructure formation. The key results of my studies are presented in the appended papers. The work has been carried out in the Thin Films Physics Division at the Department of Physics, Biology, and Chemistry (IFM) at Linköping University, and at Frederick Seitz Materials Research Laboratory and Materials Science Department at University of Illinois at Urbana-Champaign. The work has been supported by The Swedish Research Council and the Swedish Foundation for Strategic Research (SSF) project Designed Multicomponent Coatings – Multifilms.

List of Included Publications

[I] **Growth of Hard Amorphous Ti-Al-Si-N Thin Films by Cathodic Arc Evaporation**
H. Fager, J.M. Andersson, J. Lu, M.P. Johansson, M. Odén, and L. Hultman.
In manuscript, 2012

Author's contribution:
I took part in the planning of the experiments and performed the depositions. I did all characterization except TEM, where I took part. I wrote the paper.

[II] **Growth and Properties of Amorphous $Hf_{1-x-y}Al_xSi_yN$ ($0 \leq x \leq 0.2$; $0 \leq y \leq 0.2$) and a-HfAlSiN/nc-HfN Multilayers by DC Reactive Magnetron Sputtering from a Single $Hf_{0.60}Al_{0.20}Si_{0.20}$ Target**
H. Fager, A.R.B. Mei, B.M. Howe, J.E. Greene, I. Petrov, and L. Hultman.
In manuscript, 2012

Author's contribution:
I took a major part in the planning of the experiments, deposited all films, performed all characterization except TEM, RBS, and SIMS. I wrote the paper.

Acknowledgements

Many great researchers, friends, and family have contributed to this work. I truly hope that I regularly tell you how much I appreciate you, but nevertheless I will take this opportunity to say it once again.

This Thesis would not have been written if it wasn't for my supervisor *Professor Lars Hultman* who offered me to join the Thin Film Physics Division during the fall of 2009. He was patient with me while I made up my mind, but he was clever enough to treat me as a member of the group from day one, making my decision really hard. Finally, I accepted, and I must say I am very glad I did! Working with you, *Lars*, has been fun and challenging, and I thank you so much for believing in me, for tireless support and encouragement during these years, for great ideas, and endless enthusiasm.

I also would like to thank my co-supervisor *Professor Magnus Odén*, who runs the successful MultiFilms project with a solid hand. Thank you for much needed support before my first international conference presentation.

Two other very important persons that I have had the pleasure to work closely with are *Professor Ivan Petrov* and *Professor Joe Greene*. *Ivan*, thank you so much for letting me come to work with you in Urbana-Champaign. Thank you for making my stays so enjoyable, for taking me bird watching, and for sharing some of your vast knowledge in this field. It is a pleasure to work with you!

Joe, your support during conferences, and our never-ending email discussions are invaluable to me. You are meticulous when writing papers which I highly appreciate. Your criticism has made me a better writer, a better presenter, and hopefully also a better scientist. Thank you also for being an expert in giving my self confidence a boost; I think you very well know that flatter is a powerful motivator.

Dr Carina Höglund welcomed me to the Thin Film group with open arms, and for that I am so grateful. Thank you for lending me your office in times of need, for giving me the opportunity to get to know *Richard* (the best barista in town), and now also *Neo*. You have become a very good friend both at work and outside,

and I consider myself lucky to have you around.

Dr Brandon Howe came into my life at a time when I needed someone like him the most. You are an amazing teacher, and you did teach me more during those weeks in May 2010 than I had learned during the previous six months. I have worked by your side when times were tough, and I am so happy that everything has worked out to the best for you. I am fully convinced our paths in research life will cross again, and I very much look forward to that day.

Dr Björn Alling and I became friends during a discussion of the Swedish system of government. Now, you are not only my favorite co-worker, but also a very close friend, and I enjoy every moment I spend with you. I am grateful, not only for the things you taught me to love (Gruyère cheese, cold coffee, and Skyr), but also that you share my passion for `texttv` and my wish for a Swedish republic. I am so glad that I can say, like the good old Klyscherizer: *Ja, du och jag vi tänker lika.*

I would like to specially thank *Hanna Kindlund* (for great travel companionship), *Emma Johansson* (for being such a good friend), *Ali Khatibi* (for putting my swedish skills to the test), *Antonio Mei* (for great collaboration to come and for nice coffees had, *muito obrigada!*), and *Christopher Tholander* (for fun days in LA).

I would like to mention a few people who have been around since my undergraduate years. The amazing people in DA-gänget 07/08 at Kårallen, especially *Jonas Birgersson* (*tack för alla loppisrundor*), and of course, *Pontus Ek*.

Two persons deserve special mentioning; *Karl Granström* and *Jonas Callmer*. You have come to be two of my closest friends, and most of my happiest moments the last years have been with you. Thank you for traveling, beer drinking and discussing, for Baljankaffe and Torsdagslunchen^{TM}, for dancing, arguing, and laughing. I love the time we spend together.

Ulrika Pettersson and *Sofia Fahlvik Svensson*, my friends in the south, whom I miss so much. I love that we take the time to meet now and then. *Ulrika*, when I loose faith in mankind I know that a few minutes talk with you will give me a glimpse of hope back. And *Sofia*; five month in a god-forsaken village in Germany bring people close. We shared both good and bad times in Aldingen, and I am endlessly happy to now that whatever, whenever, wherever, you are just a phone call away.

Ylva Jung, *Stina Lundell*, *Oskar Leufven*, *Maja Forsberg*, *Martin Skoglund*, and *Maria Andersson*. Just thank you for being around!

Finally, but of course most importantly; my family. My little brother *Nils*, I tried to figure out something to write, but how do you find the words to thank someone who has been around for as long as you remember? I just want to tell you how much I love you, and let you know how proud I am to be your sister.

Mamma och pappa. Thank you for everything! You are such a source of inspiration to me, and I am so glad that you have the courage to follow your dreams, whatever they are. *Mitt hem är där mitt hjärta är. Jag älskar er så mycket.*

Hanna Fager
Linköping, July 2012

Contents

CHAPTER 1

Introduction

Without too much exaggeration, I dare to say that thin films are *everywhere* in modern society. We get in contact with them on an every day basis; most of the time without even realizing they are there. In fact, in terms of production economy the thinner the films are, the better, as long as the functionality is retained.

From an industrial point of view, thin films are already of major importance, and their importance keeps growing. Thin films have made it possible to increase productivity by extending cutting tool life as the thin films, or coatings, keep getting better and better, and more advanced to meet the needs in specific applications. Thin films are often applied in electrical contact applications as a way of increasing lifetime of the contacts, as noble materials that are commonly used wear rapidly.

However, thin films do not only exhibit properties that are desired for industrial applications. Without claiming that thin films change our lives, they most certainly make them much more convenient. As already mentioned, thin films are all around us; in microelectronics in cell phones, as coatings on non-stick frying pans, as protective coatings in milk cartons, as reflective coating on CDs, as anti-reflective coatings on glasses, as decorative coatings, etc.

Even though many of the examples listed above are inventions of the 20^{th} century, the idea of using thin films, or coatings, is not new. Mankind has used coatings for thousands of years. Glazed stoneware was used already in the 15^{th} century BCE in China, and the same basic idea still applies today, namely to combine the properties of a bulk material with the surface properties of another material.

The development of the first coated cutting insert was all about this. Sandvik Coromant produced the first commercially available coated cutting tools in 1969. It was called the *gamma coating* and consisted of a cemented carbide insert coated with fine-grained TiC [1]. The cemented carbide insert itself already provided

good toughness, but lacked in wear resistance. With the applied coating, the wear resistance was increased radically. After the first coated cutting tool, a number of improved coated tools found their way to the market during the 70s, 80s, and 90s. The area has expanded greatly over the last decades and the development is still ongoing.

1.1 Aim of the Thesis

This Thesis explores amorphous transition metal nitrides for cutting tool applications. It handles two different, but related materials systems: Ti-Al-Si-N and Hf-Al-Si-N. They both belong to the transition metal nitride systems, meaning that they are ceramics. Ceramics can be metallic, semiconducting or insulating and have properties such as high melting point, high hardness, and good oxidation resistance. Transition metal nitride systems have been widely studied for decades, but still, there are several areas that are not fully understood or even explored yet. One of these areas contain the amorphous transition metal nitrides.

More commonplace amorphous materials are silica-based glass. These are the most familiar type of glass, and they are what we usually refer to as ordinary glass (windows, tableware, light bulbs, jars, etc). The atomic structure of silica-based glasses lacks long range order, but possesses a high degree of short-range order with respect to the tetrahedral arrangement of oxygen atoms around the silicon atoms. Glass in general exhibits an atomic structure that resembles the one of supercooled liquids, but has the mechanical properties of a solid. Silica-based glass has been used by mankind for thousands of years, and it has been thoroughly studied. Nevertheless, there are areas that are not yet fully understood. For example, the nature of glass and the glass transition has been called *the deepest and most interesting unsolved problem in solid state theory* [2].

Metallic glasses, also called amorphous metallic alloys, have been studied since the 1960s. From the beginning they were produced through rapid quenching of melts, and in order to achieve fast enough cooling rates, they were limited to relatively small sizes. Later, multi-component composition design made it possible to produce thicker glasses, so-called bulk metallic glasses [3]. Increasing interest in these materials led to the development of thin film metallic glasses during the 1980s and 90s. Multi-component thin film metallic glasses were shown to readily become amorphous in the as-deposited state. Preparation by techniques like sputtering or evaporation, where the film condensate from the vapor phase rather than by melting and casting processes, is expected to be farther from equilibrium and thereby enable amorphous growth over a wider range of compositions.

Recently, there have been studies reporting on amorphous carbides [4–6], where the focus has been to explain the structure, chemical bonding, and structural properties of the thin films, both by experimental studies as well as by theoretical calculations. The bonding chemistry in carbide systems, where the crystalline phases exhibit structural units with carbon atoms in both octahedral and prismatic sites, is believed to be part of the explanation why carbides have a tendency of forming non-crystalline phases. However, a full explanation is still lacking.

Amorphous nitrides are just as complex as other glassy materials, but possibly even more rare amongst the ceramics, and knowledge about growth and characterization of amorphous nitride thin films is very limited. There have been studies of alloyed amorphous transition metal nitrides for application as Cu diffusion barriers on Si device layers [7–13]. There have also been studies on amorphous Zr-Si-N with high hardness and good oxidation resistance, as well as good thermal stability [14,15]. Most of these studies were conducted during the late 90s and early 00s, and the structure was assessed mainly by x-ray diffraction, which is a technique that is insensitive to crystallites smaller than a few nm.

The demand on hard, dense films for cutting tool applications in combination with the complexity of the materials systems, make the growth of amorphous nitride films a difficult process, that involves temperature, deposition rate, and ion bombardment during growth. All parameters will have to be chosen with care in order to meet the requirements. Here, also the deposition technique comes into play, and in this Thesis I have employed two different techniques: cathodic arc evaporation and reactive dc magnetron sputtering.

My materials systems of interest are based on transition metal nitrides, which are known for having a wide range of properties that are desirable in cutting tool applications. They are hard, have excellent scratch and abrasion resistance, low friction coefficient, and many of the transition metal nitride based alloys exhibit age hardening. However, transition metal nitrides form strong bonds, which is a prerequisite for hard materials, but that also means that they are likely to form crystals. In this work I have chosen materials systems in which the constituent elements have large differences in atomic size, and the equilibrium parent compounds have very different structural coordination. In combination with carefully chosen deposition parameters including low temperature kinetically-limited growth and high deposition rates, this should be a successful route for the fabrication of amorphous transition metal nitrides.

However, low temperature growth and high deposition rates come with the risk of obtaining porous films, which would make the films useless for cutting tools. Densification of the films can partly be reached by bombarding the film with energetic species during growth, but the increased adatom mobility that follows could lead to crystallization, as the atoms would be given the possibility to find equilibrium positions in the lattice.

The aim of this Thesis is to contribute to extended knowledge on amorphous nitride thin films, to describe the growth process, and to explore ways of characterizing the thin films in order to investigate the properties of these novel complex materials.

1.2 Outline of the Thesis

The Thesis starts with a detailed description of the two different deposition techniques that were used in this work. The effect of substrate bias voltage is discussed and the term sputter yield amplification is explained. Chapter three starts off with a description of film microstructure, and continues with a part about formation of

amorphous films. In addition, different materials for hard coatings are presented with respect to chemical bonding, as well as the thermodynamically stable phases of the equilibrium parent compounds of interest in this work. Then a chapter about phase stability, nucleation and growth, spinodal decomposition, and age hardening follows. The fifth chapter is about the different characterization techniques used in this work, followed by a summary of the included papers in chapter six. Finally, an outlook and future work is presented in chapter seven.

CHAPTER 2

Methods for Thin Film Synthesis

Thin films can be grown in numerous ways, where two of the main deposition techniques are chemical vapor deposition (CVD) and physical vapor deposition (PVD). Both of these techniques require vacuum to avoid reactions with the atmosphere, but also for control of composition and microstructure of the films.

In CVD, the film is grown by allowing deposition species, supplied in gas phase, to react and form bonds with the atoms at the substrate surface at conditions near thermal equilibrium. This process generally needs to take place at high temperatures ($\sim$1000 °C), which limits the use of heat-sensitive substrates. In CVD, all areas in contact with the gas will be coated, which make this technique very well suited for coating of complex shapes. Today, CVD is the most commonly used technique in hard coatings industry, even though the fraction of coatings deposited by PVD is steadily increasing.

In very general terms, PVD can be described as the process when a coating material is vaporized from a solid or liquid material source, and then condensates onto the substrate. PVD can only deposit films line-in-sight, but generally operates at much lower temperatures than CVD, which in combination with high deposition rates enables the formation of metastable structures, as the atoms may not have time and energy to rearrange in the most energetically favorable positions. This is crucial, e.g., for the formation of amorphous thin films.

Among the available PVD techniques, the two most important methods are evaporation and sputtering. The difference between these two types of PVD processes is that in sputtering, atoms are dislodged from the target surface by impact of gaseous ions, while in evaporation, the atoms are removed by thermal means [16].

In this study, two different PVD techniques have been employed; *cathodic arc evaporation* and *reactive dc magnetron sputtering*, both described in detail below.

2.1 Magnetron Sputtering

Basics of Sputtering

Figure 2.1 represents a simplified cross section of a sputtering system consisting of a vacuum chamber, a target (the source material) connected to a voltage supply, substrates, vacuum pumps, and a gas inlet for the sputtering gas.

By applying a negative voltage to the target, an electric field will form between the target and the substrate. A sputtering gas (in this case Ar) is let into the chamber. A small amount of ions and electrons will always be present in the chamber due to cosmic radiation, and these will be affected by the electric field. The electrons are repelled by the negatively charged target, and if they gain enough energy from the electric field, they will cause ionization of the sputtering gas.

The positively charged Ar ions will be attracted towards the target, where they collide with the target surface causing numerous collisions to take place. Mainly neutral target atoms are removed by momentum transfer, but other particles as secondary electrons, reflected ions and neutrals, and photons, are also scattered from the surface. The neutral target atoms travel through the chamber, where they spread in a $\cos^n \theta$-distribution, meaning that most of the target atoms will be sputtered in the forward direction where the substrate holder should be placed so that the major part will condense on the substrate to form the thin film. Some of the target atoms, however, will be ionized, and they will travel through the plasma, hitting both the grounded chamber walls and the substrate holder.

The secondary electrons are accelerated away from the target surface. These electrons help sustain the glow discharge by ionization of the sputtering gas atoms, which in turn bombard the target and release more secondary electrons in an avalanche process. When the number of generated electrons is high enough to produce ions that in turn regenerate the same number of electrons, the discharge is self-sustaining and the gas begins to glow. The light emitted is characteristic of both the target material and the incident ions.

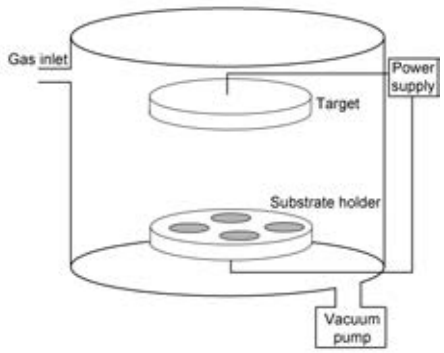

Figure 2.1. Schematic image of a sputtering system consisting of the vacuum chamber connected to a vacuum pumping system, a power supply, and an inlet for the sputtering gas. The substrate holder is facing the target.

Reactive Sputtering

Reactive sputtering refers to the process where a reactive gas is introduced in the chamber. Adding a reactive gas makes it possible to form complex compounds between the sputtered target atoms and the reactive gas molecules. This was done in Paper II, where Hf-Al-Si-N thin films were deposited by reactive sputtering from a $Hf_{0.6}Al_{0.2}Si_{0.2}$ target in an N_2-Ar gas mixture. Nitrogen is a common reactive gas, but also oxygen is much used, as well as C_2H_2 and CH_4 for synthesizing carbides. The sputtering gas does not necessarily have to be Ar. Other noble gases as Ne, Kr, and Xe can also be used, even though Ar is the most common one. It is also possible to sputter in the pure reactive gas, without any addition of a sputtering gas.

Magnetron Setup

Glow discharges are relatively inefficient ion sources. There is a high risk that the electrons will hit the grounded chamber walls, leaving the system, instead of colliding with the sputter gas atoms and ionize them. Only a few percent of the gas atoms in a glow discharge are actually ionized. By applying a magnetic field close to the target, using a so-called magnetron, the time the electrons spend in the vicinity of the target can be multiplied and the plasma is much easier maintained. This was first discovered by Penning [17] in 1936, and further developed by Kay and others [18,19]. By 1975, the magnetron sputtering technique was commercially used [20].

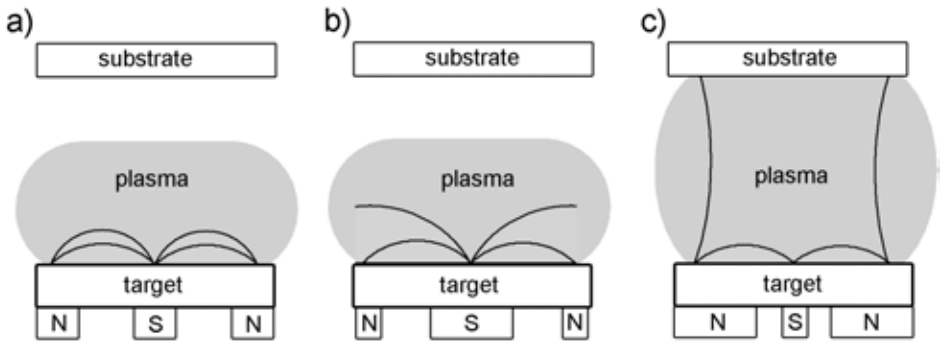

Figure 2.2. Schematic image of three different planar magnetron configurations with the magnetic field lines indicated. a) balanced magnetron, b) unbalanced type I, and c) unbalanced type II.

Several different geometries can be used for the magnetron. In this study a planar magnetron was used. The magnets are placed so that there is at least one closed path or region in front of the target surface, where the magnetic field is normal to the electric field.

There are three types of magnetron configurations available – balanced magnetrons, and unbalanced type I and type II, see Figure 2.2. In a balanced mag-

netron, the inner and outer magnets have the same strength, which confines the plasma and electrons close to the target surface. In unbalanced mode, the inner and outer magnets have different strength, where type I refers to a stronger inner magnet, whereas type II has stronger outer magnets.

In Paper II a modified type II unbalanced magnetron was used. This system was developed and characterized by Petrov et al. [21]. It is a regular UHV planar magnetron system with a pair of Helmholtz coils that enables application of a variable external axial magnetic field, B_{ext}. This external magnetic field is superimposed on the permanent magnetic field of the magnetron.

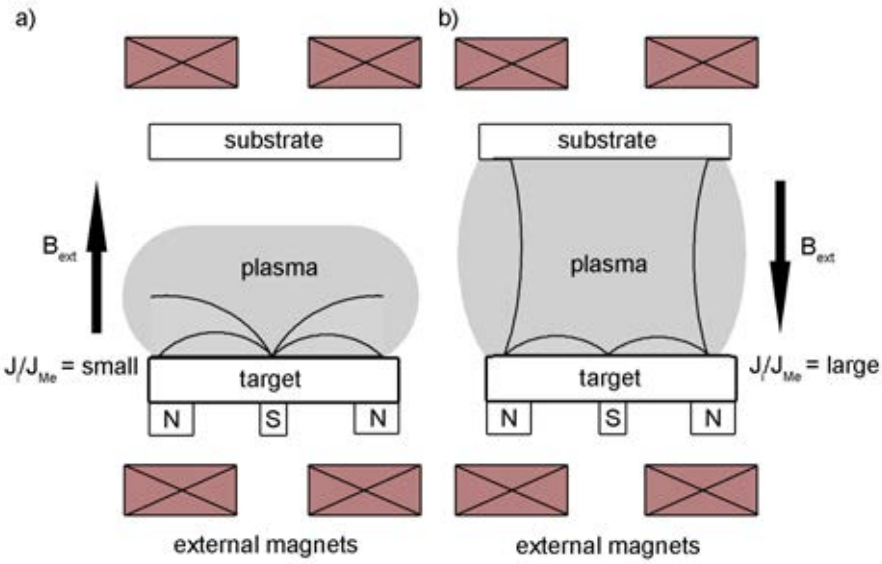

Figure 2.3. Schematic image illustrating the effect on the plasma of superimposing an external magnetic field B_{ext} which a) opposes, and b) reinforces the field of the outer permanent magnets in the magnetron. After Petrov et al. [21]

The external magnetic field can be negative or positive with respect to the outer permanent magnets in the planar magnetron. If the external field is negative, the field between the target and the substrate will have the same sign as the central pole, meaning that the electrons will be steered away from the substrate towards the walls of the chamber, reducing the plasma density near the substrate, and thus reduce the ion-to-metal-flux ratio, J_i/J_{Me}, on the growing film, see Figure 2.3. A positive field leads to an increased fraction of electrons that escape the trap over the target, and they are channeled towards the substrate. This increases the plasma density close to the substrate and enhances the ion flux incident at the growing film. The ion-to-metal-flux ratio, J_i/J_{Me}, was shown to vary with B_{ext}, without any significant effect on the ion energy, E_i. This enables independent control of the ion flux and the ion energy, meaning that it is possible to control the degree of unbalancing of the magnetron.

The Effect of Substrate Bias Voltage

Negative substrate bias voltages can be applied from an external power source, and the growing film will then be subjected to positive ion bombardment. Other energetic particles, such as secondary electron, ions that have been reflected from the sputtering target and are now neutrals, and photons are also irradiating on the growing film.

By introducing a bias voltage, the electric fields near the substrate are modified in order to vary the energy and flux of the incident particles. The application of a bias voltage can change the film properties in several ways; it affects residual stresses, film morphology, density, grain size and preferred grain orientation; improves adhesion to the substrate; increases oxidation resistance in optical films; enables control of magnetic anisotropy; increases dopant incorporation probability; and most importantly for this work: enables control of film composition [16, 22].

Applying a substrate bias voltage is an effective way of tailoring film properties by quite simple means. However, the effect is complex and it is not only the incident ion energy (E_i) that must be considered, but also the incident ion flux, J_i, the mass of the incident ions, m_i, and the growth temperature T_s. When energetic particles bombard the substrate surface during film formation this leads to higher surface mobility of adatoms and elevated film temperatures, which has consequences for atomic reactions and interdiffusion rates, and is of special importance for amorphous film formation.

For controlling the growth kinetics and the physical properties of thin films, low-energy (E_i <100 eV) ion bombardment has been shown to be useful [22]. Ion bombardment during growth is used to control composition of the growing film when sputtering from an alloy target. The control is performed through sputter yield amplification.

Sputter Yield Amplification

The term sputter yield amplification (SYA) was introduced by Berg and Kartadjiev [23]. It is based on preferential re-sputtering of lighter species during ion bombardment of alloys, leading to enhanced sputter yields of lighter elements as compared to the elemental ones.

To understand the preferential re-sputtering effect it is important to have basic knowledge about the sputter yield of elements. The sputter yield is defined as the number of atoms ejected from the target surface per incident ion [24]. It is one of the most fundamental parameters of the sputtering process, but still are not all effects that contribute to the sputter yield fully understood. The sputter yield of an element increases with increasing incident ion energy, but also increases with increasing mass and d-shell filling of the incident ion [25, 26]. Sputter yields for many elements can be found in the literature, however, the sputter yield for an element can vary substantially if it is sputtered from a pure elemental target or from an alloy. For the elements used in this study, the sputter yield at 300 eV Ar^+ bombardment is 0.65 for Al, 0.31 for Si, 0.33 for Ti, and 0.48 for Hf [27].

When sputtering from an alloy target, the initial bombardment will cause the element with highest sputter yield to be removed first. The target will then be

enriched in the material with lower sputter yield. At steady state, the composition of sputtered species is equal to the target composition [28].

SYA describes the compositional enhancement of an element with higher mass m_h as compared to an element with lower mass m_l due to bombardment by ions with intermediate mass m_i. In Paper II we deposited films consisting of elements with large difference in mass (Hf = 178.49 amu, Al = 26.98 amu, and Si = 28.09 amu) as compared with the mass of Ar^+ = 39.95 amu.

Ar^+ ions will be the primary energetic species that hit the growing film. They will have energies $E_i = eV_s$, where $V_s = (V_{plasma}\text{-}V_a)$, and V_{plasma} is the plasma potential, and V_a is the applied substrate bias potential. The energy transfer from an impinging Ar ion to the growing film happen as follows: first of all, the maximum energy transfer occurs during 180° backscattering collisions. If the ion collides with a Hf atom, the energy transfer can be estimated as [29]:

$$\frac{4 \cdot m_{Hf} \cdot m_{Ar}}{(m_{Hf} + m_{Ar})^2} E_i \tag{2.1}$$

This means that ∼0.6E_i is transferred to the Hf atom, meaning that the Ar ion is backscattered with an energy $E_b \approx 0.4E_i$. If the Ar ion instead collides with an Al or Si atom it will transfer ∼96-97% of its energy and is reflected with $E_b \approx$ 0.03-0.04E_i.

This extremely efficient energy transfer to the lighter elements, leads to re-sputtering of Al and Si as an Ar ion first collides with a Hf atom in the film, is backscattered, and collides with an Al or Si atom on the way out. However, the energy of the reflected ion, E_b, must be high enough for preferential re-sputtering of Al and Si, but below the Hf sputtering threshold.

In Paper II this effect was used to vary the composition of the films by just changing the incoming ion energy, E_i.

2.2 Cathodic Arc Evaporation

As already stated; in evaporation techniques the atoms are removed by thermal means. Both evaporation and sputtering techniques derives from the mid-nineteenth century. The development of better vacuum-pumping equipment and heating sources, spurred the process of evaporation techniques, even though sputtering was also used on an industrial scale meanwhile [16]. Until the late 1960s, evaporation was the preferred deposition technique, due to high deposition rates, good vacuum, and the possibility to deposit all kind of materials.

In arc evaporation a discharge between two electrodes is used to melt and evaporate the material. The cathode corresponds to the target in sputtering, and consists of the material that will be deposited. The high current, low voltage discharge melts a small spot on the cathode surface creating a plasma discharge. A current flows from the small spot, the so-called cathode spot. At the local spot the temperature is high enough to melt the target material and neutral atoms, electrons, and ions, are evaporated. There can be one or more active arc spots on the cathode surface, but due to heating of the cathode at the local spot, the

resistivity increases. If several spots are active at the same time, the newer spot will be preferred due to lower resistance.

To start the process the arc has to be ignited. A common way is to let a mechanical trigger create a short circuit on the cathode side which gives a short, high voltage pulse. Since the cathode and the anode are largely separated in the system, a conductive ionized gas, a so-called plasma, is created. The plasma make the process self-sustained since the electrical current that flows between the cathode and the anode is transported by the plasma [30].

The electrons are attracted by the electric field, and they collide with evaporated atoms and ionize them, in the so-called ionization zone. The ions are then transported to the substrate surface where they condensate to form the growing film. Figure 2.4 shows a schematic illustration of the arc process.

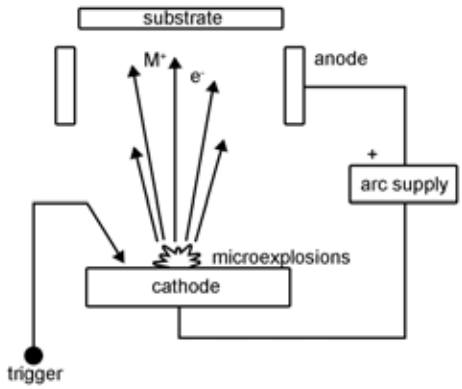

Figure 2.4. Schematic image showing an arc process.

In contrast to the case in magnetron sputtering, the plasma is highly ionized in arc evaporation. Close to the cathode spots the degree of ionization is nearly 100% [30]. The plasma can be manipulated using electric and magnetic fields [31]. This can be used to change the stoichiometry of the films when growing from a compound target, since different elements have different degree of ionization. Ions with high degree of ionization will impinge on the film surface with higher energy, thus penetrating deeper into the film and cause preferential re-sputtering of light elements in the growing film. A high degree of ionization also provides high deposition rates, which makes it possible to grow dense films with good adhesion [32].

In the same way as in reactive magnetron sputtering, *reactive* cathodic arc evaporation can be performed by introducing a reactive gas into the chamber. Light elements like carbon, oxygen or nitrogen are often introduced in the gas phase, but they can also be introduced via the cathode [33]. Compound cathodes can be used to control and vary the composition of the films.

In industrial arc evaporation systems, there is usually room for several cathodes. Figure 2.5 shows a schematic illustration of the industrial system used in

Paper I. In this system, cathodes can be placed both left and right of the door to the deposition chamber, but also on the door itself. The substrates are mounted on a rotating drum in the center of the system.

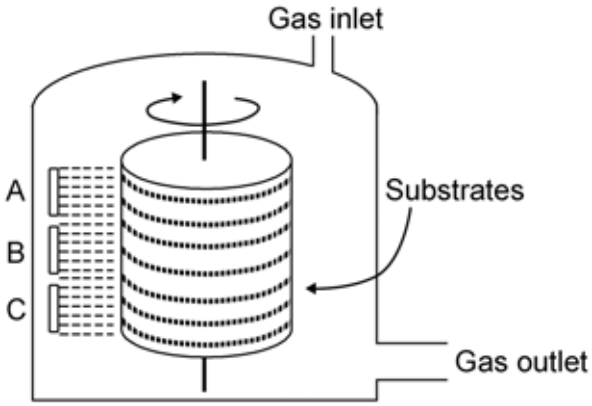

Figure 2.5. Schematic image illustrating the industrial arc evaporation system used in Paper I, with cathode positions A, B, and C, on one side of the deposition chamber, and a rotating drum holding the substrates.

In Paper I, three 63 mm diameter cathodes were aligned vertically on the wall of the deposition chamber (position A, B, and C), with compositions: $Ti_{0.75}Si_{0.25}$, $Ti_{0.23}Al_{0.47}Si_{0.30}$, and $Ti_{0.75}Al_{0.25}$, respectively. This arrangement enabled variations in the film compositions depending on the position of the substrates in relation to the cathodes. By arranging the cathodes in this way, the plasma generated from each cathode will partly overlap. This can be used to grow films with a wide range of compositions during one deposition. But if the drum holding the substrates is rotating, this can cause compositional modulation that is visible as layering in the films. This layering effect was seen in Paper I, where also the composition of the films indicate that the plasmas have been overlapping. This effect is described in detail by Eriksson et al. [33].

When the material is melted and evaporated larger particles, so-called droplets, are ejected. These droplets are incorporated in the growing film. The droplets hinder the growing film, and they can serve as nucleation sites for differently shaped grains that can grow large in size. The presence of these macroparticles causes increase in the surface roughness.

CHAPTER 3

Thin Film Growth

Thin film growth is a phase transformation, where vaporized atoms condensate and form a solid film. All such phase transformations involve a nucleation and growth process.

When the sputtered species arrive at the substrate, they move on the substrate surface and gather to form small clusters or islands. These islands are more or less evenly distributed over the surface. Impinging atoms are drawn to the islands that grow larger and increase in density. The coalescence of the islands decreases their density and creates uncovered areas on the substrate where nucleation can continue [16]. Finally the islands merge into a film.

3.1 Microstructure

The mobility of the adatoms on the surface determines the microstructure of the growing film. If the surface diffusivity is high, the adatoms are able to travel greater distances and form large grains. If the surface diffusivity is low, the adatoms will be trapped at low-energy lattice positions, creating many nucleation sites at the substrate. These nucleation sites will grow individually and form a columnar structured film. A way of illustrating the effect of deposition parameters on the resulting structure is often done in a so-called structure zone diagram (SZD). These diagrams were developed for evaporation in 1969 [34], and for sputtering in 1974 [35]. A diagram for plasma-based depositions was presented more recently [36], see Figure 3.1.

The structure zone diagram for plasma-based depositions describes the microstructure as a function of the generalized temperature T^*, the normalized energy E^*, and the net film thickness t^*. The generalized temperature includes both the homologous temperature T_h, which is the ratio of the deposition temperature

T_s over the melting temperature T_m in K, and a temperature shift that is caused by the potential energy of the particles arriving on the surface. The normalized energy E^* describes the displacement and heating effects that are caused by the kinetic energy of particles bombarding the surface, e.g., when the substrate is biased. The net film thickness illustrates the microstructure of the films as they grow, and also show the effect of densification of the films, as well as possible ion etching.

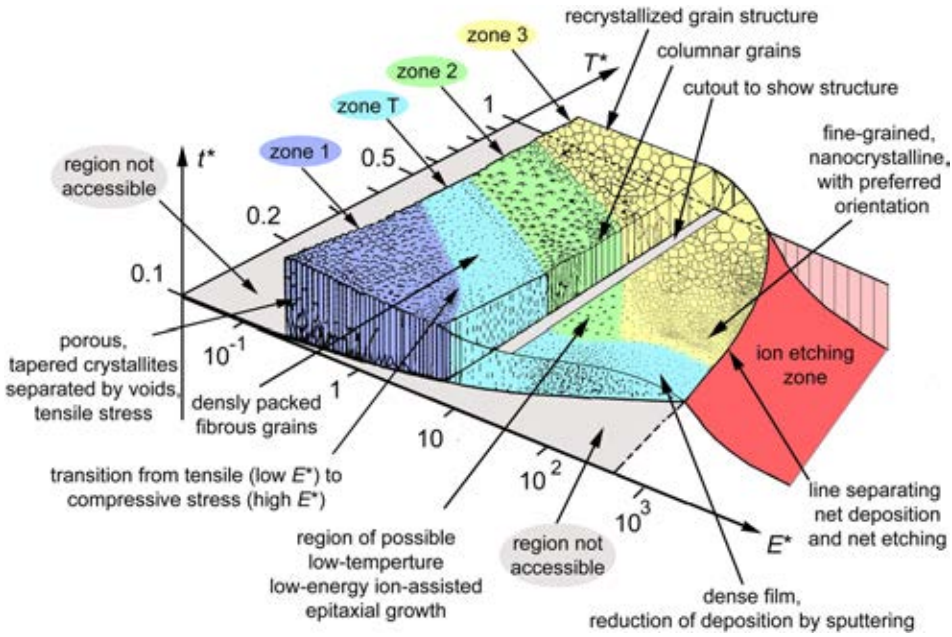

Figure 3.1. Structure zone diagram for plasma-based thin film deposition from Anders [36]. © 2010 Elsevier B.V. Reprinted with permission.

The diagram suggested by Anders [36] is divided into four zones, where Zone 1 represents growth at low temperatures and low energy. Here, the adatom mobility is low which favors growth of textured porous films. Zone T is a transition zone, where the surface diffusivity is improved compared with zone 1, but it is limited over grains boundaries, which lead to V-shaped grains. In zone 2 the surface diffusivity is higher and not limited by grain boundaries, thus leading to uniform columnar grain growth. Zone 3 involves high temperature and high energy where bulk diffusion is allowed and recrystallization and densification of large grains occur.

It should be noted that this diagram is adapted for polycrystalline films. Also, the intention of the structure zone diagrams is to give a simplified description of tendencies rather than to be an accurate tool for structure prediction. Growth of amorphous films is highly dependent on the deposition rate. In very general terms high substrate temperatures and low deposition rates is associated with large grains or single crystals. And the other way around; low substrate temperatures

and high deposition rates yield polycrystalline or even amorphous films. According to the structure zone diagrams a necessary (but not sufficient) condition for formation of amorphous phases is that T_h is smaller than 0.3. For higher values, the surface diffusion of the deposited species will allow for crystallization.

3.2 Formation of Amorphous Films

The word *amorphous* comes from the Greek, and is a combination of *a* meaning without, and *morphé* meaning shape or form. The term amorphous solid has no defined structural meaning, but Kittel describes it as *"not crystalline on any significant scale"* [37]. In condensed matter physics, amorphous refers to a solid that lacks the long-range order that is characteristic for crystals.

Even though amorphous materials lack long-range order, they have a structure that exhibit short-range order in regions where the placement of the atoms can be predicted [16]. This means that the atom positions are not totally uncorrelated as in an ideal gas, where each atom may be located anywhere, but there is a local correlation where each atom has its nearest-neighbor atoms at nearly the same distance to it. Also, the bond angles are almost equal as in the crystalline preferred phase [38].

For a long time, it was thought that only a limited number of materials could be prepared in the form of amorphous solids, and amorphous metals were not believed to exist. But in the mid-50s pure metal Ga and Bi films were produced [16], and soon it was realized that there were no specific glass-forming solids. Rather, it is a question of how the solids were produced, and Turnbull expressed it as: *Nearly all materials can, if cooled fast enough and far enough, be prepared as amorphous solids.* [38]

For amorphous solids it becomes a profound practical problem of realizing extremely fast cooling rates (from 1 K/s for oxides to $>10^6$ K/s for elemental metals) for a given volume. For thin film, fast cooling rates are not a concern since the film condensate from the vapor phase. On the other hand, for growing amorphous thin films, the atoms need to be hindered from finding their equilibrium positions in the lattice. This requires high deposition rates and low substrate temperatures. Low substrate temperatures freezes the impinging adatoms on the substrate and prevents them from diffusing and finding equilibrium lattice sites. High deposition rates mean that the atoms will not have time to move far on the substrate to find such favored positions before yet another adatom arrives at the surface. The atoms will thus be trapped in unfavorable positions and are covered in the growing film. There are ways to affect the growth, not only by lowering the deposition temperature. Large doses of implanted ions on the growing film can also amorphize surface layers by momentum transfer, layers that otherwise would be crystalline.

In general, the formation of amorphous phases is promoted in alloy systems where (1) the heat of mixing is strongly negative, hence in systems with strong tendency for compound formation, (2) there are large differences (>10%) in atomic size, and (3) deep eutectic points exist on the phase diagram [39, 40].

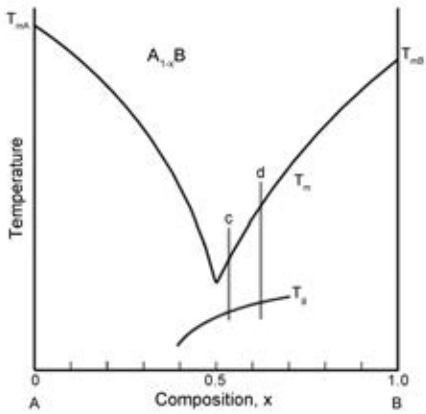

Figure 3.2. A simplified binary phase diagram of a hypothetic alloy $A_{1-x}B_x$ with a deep eutectic point.

The trend is that the glass-forming ability tend to be larger for binary materials than for elemental ones. The components in a binary alloy hinder the mobility of each other, but this effect is also attributed to the relation between the glass transition temperature T_g, and the freezing or melting temperature T_m. Figure 3.2 shows a phase diagram for a binary system, $A_{1-x}B_x$ $(0 < x < 1)$. For the alloy, the liquid is stabilized and the melting point T_m is lowered as compared with the single-element end points $x = 0$ and $x = 1$. There is a eutectic composition at $x = 0.5$ at which the melting point T_m is minimized. Near the eutectic composition, at point c in the figure, the liquid is much more readily quenched to the glass phase than at a composition corresponding to point d, since the distance between T_m and T_g is much larger at d than at c. The distance is even smaller at the eutectic composition, meaning that this composition would be favored for formation of amorphous solids.

Most amorphous alloys fall into one of four categories [16]:

- transition metals and 10-30 at% semimetals
- noble metals and semimetals
- early transition metals in combination with late transition metals
- alloys consisting of IIA metals

Since the principal structural order in amorphous solids is determined by the separation between nearest-neighbor atoms or molecules, it is extremely hard to distinguish between amorphous and crystalline structures on this length scale, even with advanced characterization techniques including x-ray diffraction and transmission electron microscopy. It is not always easy to resolve whether so-called amorphous films are in reality nanocrystalline. In the two papers appended in this

Thesis two terms are used; x-ray amorphous and electron-diffraction amorphous. X-ray amorphous films are defined as films where no diffraction peaks are visible. Electron-diffraction amorphous films show a diffuse halo in electron diffraction, and no presence of nanocrystalline grains in HRTEM.

3.3 Materials for Amorphous Hard Coatings

In the papers in this Thesis the aim has been to grow electron-amorphous transition metal alloys with both high hardness and high toughness for potential use in cutting tool applications. Two different materials systems have been investigated; Ti-Al-Si-N and Hf-Al-Si-N in which the constituent elements have large differences in atomic radii (N 0.065 nm, Si 0.110 nm, Al 0.125 nm, Ti 0.140 nm and Hf 0.155 nm [41]), as already mentioned an important factor for formation of amorphous compounds. In addition, the equilibrium parent compounds – HfN, TiN, AlN, and Si_3N_4 – have very different structural coordination.

Figure 3.3 shows the chemical bonding for some common hard materials. As seen in the figure, ceramics have mixed bonding type. Bonding in NaCl-structure transition-metal nitrides, like TiN and HfN, involves a combination of metallic, covalent, and ionic contributions [42], whereas Si_3N_4 and AlN consist of a mixture of covalent and ionic bonding.

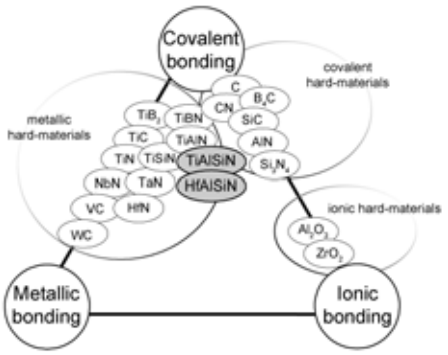

Figure 3.3. Hard materials, classified after chemical bonding, adapted from Mayrhofer et al. [43]

Metallic bonds are formed due to attractive forces between positively charged metal ions and negatively charged delocalized valence electrons that are gathered in an electron cloud that moves freely across the material. Metallic bonding is the reason for many properties of metals, such as strength, ductility, thermal and electrical conductivity, among other.

Ionic bonding is formed in materials with charged particles, where the attraction between the positive cations and negative anions holds the solid together.

Generally, ionic bonds form between very active metallic elements and active non-metals. However, there is no such thing as pure ionic bonding and all ionic compounds have some degree of covalent bonding. The covalent type of bonding is characterized by the sharing of electron pairs between the atoms, and there is a stable balance of attractive and repulse forces between the atoms [44].

TiN and HfN

TiN is one of the most well known and most studied materials for thin films, and it has been commercially available as a protective coating on cutting tools since the 1970s. Today, there are several alternatives in the area of protective coatings, with better oxidation resistance, higher hardness, etc. Nevertheless, TiN is still a common coating, and it is also used for decorative purposes because of its yellow color that resembles the color of gold. TiN_x is thermodynamically stable over a wide range of compositions, $0.6 < x < 1.2$ [42].

HfN on the other hand, is a much less studied binary nitride. It is known to be the most refractory of all known nitrides, with a melting point of 3310 °C and it has a high hardness (H = 23.5 GPa) [45].

Ti and Hf, like many other transition metals, are crystallized in the cubic rock salt structure with nitrogen if the metal-to-nitrogen ratio equals unity. The rock salt structure can be described by a fcc Bravais lattice with a basis of two atoms (metal and nitrogen). In the structure, pictured in Figure 3.4, the metal atoms occupy the octahedral sites, and each metal atom is coordinating six nitrogen atoms.

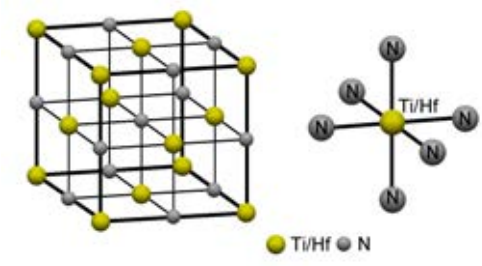

Figure 3.4. NaCl-structure of TiN/HfN where Ti or Hf atoms occupy octahedral sites, coordinating six N atoms.

AlN

AlN is a wide band gap semiconductor that is much used in optical and microelectronic device applications. Aluminum nitride is stable at high temperatures, but in air it oxidizes at 700 °C and forms a protective surface layer that is stable up to 1370 °C.

The thermodynamically stable phase of AlN is wurtzite, which is a hexagonal structure. However, there is a metastable zinc-blende AlN phase [46], as well as a

metastable rock salt AlN phase at high temperates and high pressures. Rock salt AlN has also been observed as an intermediate phase during spinodal decomposition [47]. In the wurtzite structure the atoms have tetragonal coordination, and the tetrahedra are arranged in such a way that each Al atom is bonded to four N atoms (and vice versa) with equal bond lengths. The metal-to-nitrogen ratio has to be unity. The wurtzite structure can be described as two hexagonal close packed lattices, one with metal atoms, and one with nitrogen atoms, that are stacked on top of each other, and one is displaced in relation to the other. The nitrogen atoms are placed so that they occupy half of the available tetrahedral sites in the metal atom lattice. The wurtzite structure of AlN is shown in Figure 3.5.

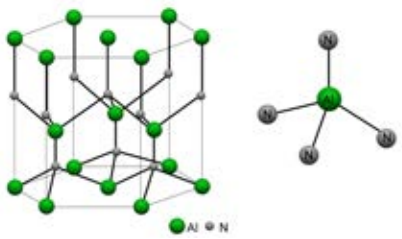

Figure 3.5. Wurtzite structure of AlN where each Al atom coordinates four N atoms and vice versa.

Si_3N_4

Silicon nitride is a hard ceramic that has an unusually high fracture toughness. It is most used in high temperature applications such as gas turbines, car engine parts, and bearings, but also on cutting tools.

Si and N form a stable compound, Si_3N_4, where the trigonal, hexagonal, and amorphous phases are the most common [48]. There is also a cubic spinel phase that only can be synthesized under high pressure and high temperature conditions [49]. The structure in trigonal Si_3N_4 is based on the SiN_4-tetrahedra. The tetrahedra are arranged in such a way that every Si atom coordinates four N atoms and every N atoms coordinates three Si atoms, see Figure 3.6.

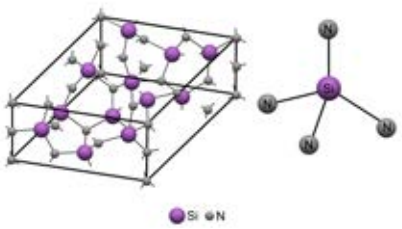

Figure 3.6. Trigonal structure of Si_3N_4 in which each Si atom coordinates four N atoms and each N atom coordinates three Si atoms.

CHAPTER 4

Phase Stability

4.1 Phase Stability and Metastable Phases

The deposited films in both Paper I and Paper II are metastable. Metastability refers to a state where the system is locally stable and might be unaffected by small fluctuations (like variations in temperature and/or pressure), but that there exist a global minimum in free energy where the system is at equilibrium. An illustration of this can be found in Figure 4.1. This can also be realized by studying the free energy diagram for a hypothetical binary alloy, $A_{1-x}B_x$, in Figure 4.2.

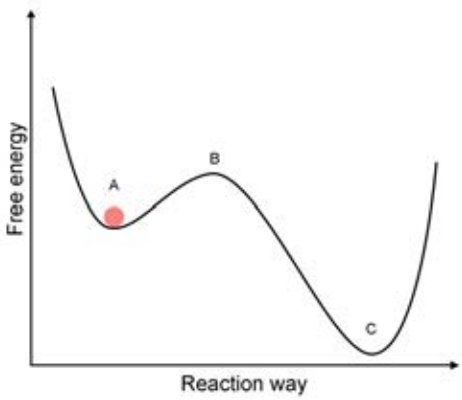

Figure 4.1. Schematic illustration of metastability. Point A is a local minimum where the system is in a metastable state, whereas point C shows a global minimum corresponding to a stable configuration. The energy barrier B must be overcome to achieve the most energetically favorable state.

To construct these diagrams one draws the molar free energy curves for each phase, α and β. Since there are variations in entropy and in electronic binding energy that vary with composition, also the molar free energy will vary. From the curve it is fairly straight-forward to see that for an A-rich alloy the α-phase will have lowest free energy, and for a B-rich alloy the β phase is most favorable. In the region near point Z the total energy might be minimized if the atoms separate into two phases. For this separation, or decomposition, to take place the atoms need to diffuse over considerable distances, and this will only happen at high enough temperatures, even if there are no other barriers for separation. The low deposition temperatures employed in PVD techniques make it possible to deposit metastable alloys far from thermodynamical equilibrium conditions.

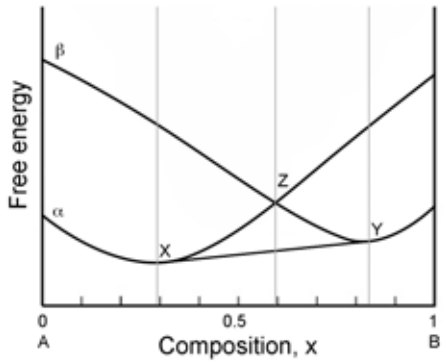

Figure 4.2. Free energy diagram of a hypothetical alloy $A_{1-x}B_x$.

4.2 Nucleation and Growth

In solid state materials, most phase transformations are a result of diffusional nucleation and growth [50]. For the hypothetical alloy system in Figure 4.2, phase β at composition X could lower its free energy if it could transform itself into phase α instead. This transformation can occur and it begins by formation of small particles, nuclei, with different phase than that of the matrix that surround them. The nuclei have to form interfaces to the matrix phase. This requires energy, meaning that the energy gain by reducing the system energy must be larger than the energy needed for forming the interfaces. When the nuclei have reached a critical size the gain in binding energy is larger than the loss in surface energy and the nuclei will start to grow. Finally, the material will consist of only the lower-energy phase.

4.3 Spinodal Decomposition

Growth by PVD makes it possible to create systems where the components normally are immiscible. It is even possible to create systems where there is no free energy barrier for nucleation. Such systems are stabilized only by diffusion barriers and are thermodynamically unstable since any local compositional fluctuations will be amplified if the films are exposed to high temperatures, for example during annealing experiments or cutting operations. This is called spinodal decomposition and means that there will be areas in the film with different composition and also different physical properties. For most crystalline solid solutions, a difference in composition comes with a variation in lattice parameter, and in order to retain the lattice structure so-called coherency strains are introduced in the material.

Figure 4.3 shows a free energy curve and corresponding phase diagram for a system with immiscible components. Alloys within the unstable, spinodal, region will undergo spinodal decomposition without any preceding nucleation [51].

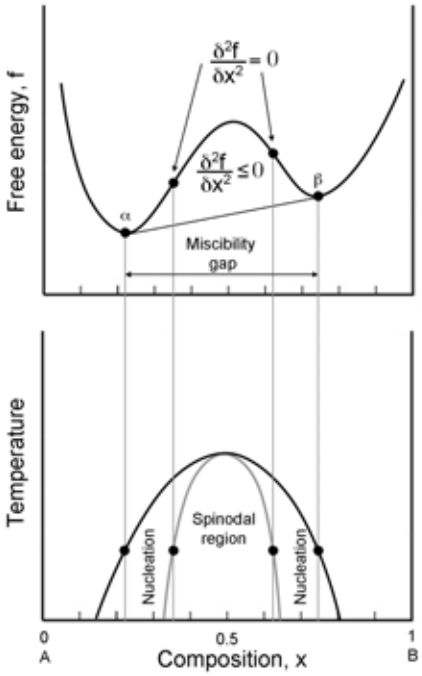

Figure 4.3. Free energy curve and corresponding phase diagram for a system with immiscible components.

4.4 Age Hardening

Age hardening is a hardening phenomenon that occurs when precipitates form in a material, for example when it undergoes phase decomposition during annealing. An example of this is found during spinodal decomposition of TiAlN [52], where cubic TiAlN decomposes into c-TiN and c-AlN, and the later finally into h-AlN. The first transformation is attributed to an increased hardness, that is lost when the hexagonal AlN is formed.

The small particles, or precipitates, hinder defect formation and dislocation movement in the material, leading to increased hardness. If precipitates are present in the matrix, dislocations will be arrested, go around, or cut right through them, which is, irrespective of which, more difficult than traveling through a homogeneous matrix. Introducing precipitates with the right size in a material is a difficult process, and in the case of too little diffusion – under aging – the particles will be to small to hinder dislocations effectively. Too much diffusion will cause formation of large precipitates that are dispersed and interact within most dislocations.

An example of age hardening in this work is found in Paper I where initially x-ray amorphous $(Ti_{0.26}Al_{0.46}Si_{0.28})N_{1.17}$ thin films show a linear increase in hardness with increasing annealing temperature up to 1000 °C, due to formation of nanocrystals in the films.

CHAPTER 5

Characterization Techniques

Several different analysis techniques and instruments are needed to determine the nature of a thin film. In this Thesis a combination of x-ray diffraction (XRD), transmission electron microscopy (TEM), scanning electron microscopy (SEM), energy dispersive x-ray spectroscopy (EDS), Rutherford Backscattering Spectrometry (RBS), Secondary Ion Mass Spectrometry (SIMS), and nanoindentation, were used to determine composition, microstructure, and mechanical properties of the films.

5.1 X-ray Diffraction (XRD)

X-rays were detected by the German physicist Wilhelm Conrad Röntgen in 1895, a detection that earned him the first Noble Prize in Physics in 1901. X-rays are electromagnetic waves with a wavelength of 0.01-10 nm, which was discovered in 1912 by another German physicist, Max von Laue. This, together with the discovery that atoms are periodically ordered in crystals and that they can scatter x-rays, earned him the Nobel prize in Physics in 1914.

X-ray diffraction (XRD) is a non-destructive technique that is much used, since there is no need for complicated sample preparation, and the evaluation is often quick and straight-forward.

XRD is based on the principle of scattering. When x-rays enter condensed matter they scatter in all directions, giving rise to constructive and destructive interference. This phenomena was first described by William Bragg and William Lawrence Bragg in 1912, which earned them the Nobel Prize in Physics in 1915. The relationship is called Bragg's law:

$$2d \sin\theta = n\lambda, \tag{5.1}$$

where d is the lattice plane distance, θ is the scattering angle, λ the wavelength of the x-rays, and n is an integer. Bragg's law states an intensity maximum for an integer number of wavelengths, see also Figure 5.1. In the case of constructive interference, intensities add up and show as peaks, while in destructive interference x-rays cancel each other.

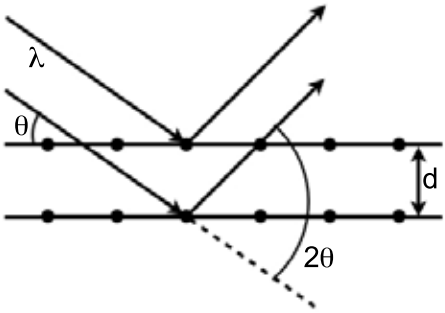

Figure 5.1. Schematic illustration of x-ray diffraction according to Bragg's law, Eq. 5.1.

In an x-ray tube electrically charged particles are accelerated towards a Cu plate from where the x-rays are emitted. By using a Ni filter at the exit of the x-ray tube, Cu K_β-radiation is filtered out, and only Cu K_α with a wavelength of 1.54 Å is left. In this Thesis, Cu K_α x-rays were used to study the films in a $\theta - 2\theta$ configuration.

In symmetric $\theta - 2\theta$ scans the incident beam angle changes at half the rate of the outgoing beam, which give peaks at characteristic 2θ values, so-called Bragg angles. The incident and outgoing beams have equal angles with respect to the sample surface, thus the scattering vector is always normal to the sample surface, meaning that only reflections from lattice planes parallel to the sample surface contribute to the peaks. Not only the peak positions, but also the shape of the peaks can give valuable information. If the sample is textured, i.e., has preferred growth in one specific lattice direction, it will change the relative height of the peaks. Also, crystalline grain size affects the peak width and it is possible to estimate the crystallite grain size using Scherrer's equation:

$$D = \frac{K_s \lambda}{\beta \cos\theta}, \tag{5.2}$$

where D is the crystalline grain size, K_s is a geometrical shape factor, λ the wavelength of the x-rays, β is the peak width (integral breadth or full width at half maximum, FWHM), and θ is the scattering angle. In Paper I, FWHM was used to calculate the crystalline grain size. Small crystalline grain sizes will give broad and diffuse peak, and if the sample consist of randomly oriented crystallites smaller than 2-5 nm, it may not be possible to detect them due to severe peak broadening. A sample like that is regarded x-ray amorphous. This was used in Paper I where the x-ray amorphous structure of the samples is evidenced by the

lack of diffraction peaks. Figure 5.2 shows an example of a diffractogram with a crystalline and a x-ray amorphous sample.

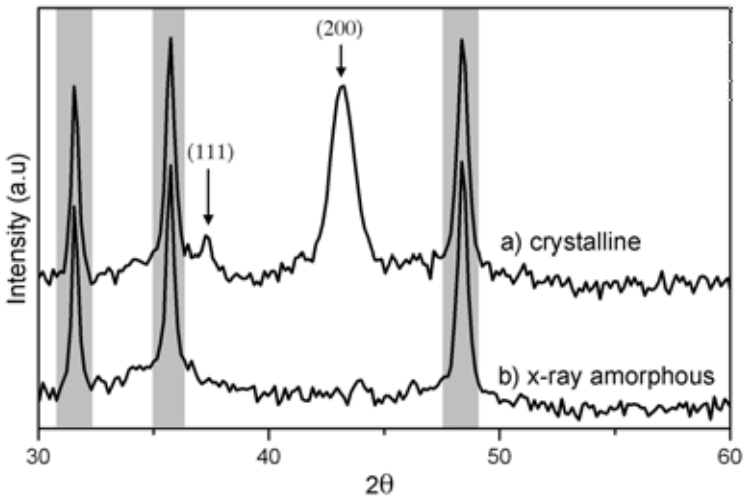

Figure 5.2. A typical diffractogram showing Ti-Al-Si-N films that are a) crystalline, and b) x-ray amorphous. Peaks underneath the grey areas correspond to the substrate peaks.

5.2 Electron Microscopy

In electron microscopy the beam that illuminates the sample consists of electrons instead of visible light, as in the case of light-optical microscopes (LOM). The resolution of a microscope can be described by the Rayleigh criterion which states the smallest distance between two objects that can be resolved:

$$d = 0.62\frac{\lambda}{n \sin\theta} \tag{5.3}$$

d is the resolution, λ the wavelength, n the refractive index of the medium, and θ the angle of the collected light. For an electron microscope operating at an acceleration voltage of 200 kV, this gives a wavelength in the range of picometers. The best electron microscopes can achieve better than 50 pm resolution [53] and magnification up to about 50.000.000x, as compared to the best light optical microscopes that are limited to about 200 nm resolution and magnifications below 2000x.

In an electron microscope electrostatic and electromagnetic lenses are used to control the electron beam and to focus it to make an image. They have the same task as the glass lenses that are used in light optical microscopes to focus the light.

5.2.1 Transmission Electron Microscopy (TEM)

In transmission electron microscopy (TEM) electrons are emitted by an electron gun and accelerated at a voltage of ∼200 keV towards the sample. The sample is thin, less than 100 nm, and the beam is partly transmitted through, and partly scattered from the sample. This gives rise to an outgoing beam with different electron intensities, that holds information about the structure of the sample. The various electron intensities are translated into contrast, and the image is projected on a fluorescent screen or recorded by sensors of a CCD camera, which can be displayed on a computer monitor.

If the electron beam just interacts with the sample and then is transferred to the screen, the result will be a low contrast image. To improve contrast, apertures can be placed in the back focal plane of the objective lens to filter away scattered electrons. Only the transmitted electrons now contribute to the image, and a bright field (BF) image with better contrast is obtained. The dominating contrast mechanism in bright field mode is the mass-thickness contrast that arises due to elastic and incoherent scattering of the electrons by the atoms in the sample. Areas that are thick, and that consist of atoms with high mass and high density will scatter more electrons, and will appear dark in a BF image.

The electrons can also be filtered in such a manner that only scattered electrons form the image. The contrast will now be inverse, and the image mode is called dark field (DF). In dark field mode the contrast occurs due to coherent scattering of the electrons at certain Bragg angles.

The third contrast mechanism is phase contrast. It requires more than one beam, and is used in high resolution TEM (HRTEM) by using a combination of the transmitted and the diffracted beam. The contrast comes from the pathway difference between the two beams when one of them is scattered. HRTEM makes it possible to get lattice resolved images.

Electron diffraction can be used to obtain crystallographic information of the sample. Diffraction occurs in the TEM in a similar manner as in XRD, but one great benefit of electron diffraction compared to x-ray diffraction is that the short wavelength of the electrons makes it possible to probe very small volumes of the sample [54]. This was the case in Paper I, where the crystallization of w-AlN could not be detected by XRD, but was detected with TEM.

When the electron beam is diffracted by the atoms in the sample, and Bragg's law is fulfilled, it gives rise to a diffraction pattern in the back focal plane. By placing an aperture in the back focal plane, certain areas on the sample can be chosen to obtain a diffraction pattern from that specific region by so-called selected area electron diffraction (SAED). SAED patterns can help to determine whether a sample is amorphous, single crystalline or polycrystalline. This is done by studying the shape of the diffraction pattern, where an amorphous sample would yield a diffuse ring pattern, a polycrystalline sample gives a clear or speckled ring pattern, and a single crystal sample would give a dotted pattern. By aligning the central beam along the zone axis, the distance between the rings or dots in the diffraction pattern and the central spot, can be used to relate the diffractions based on the Miller indices of the planes from which the respective diffraction origins.

In STEM, scanning transmission electron microscopy, the electron beam is focused to a probe that is scanned across the sample. The information is collected in each spot and in combination with a high-angle annular dark-field detector (HAADF), that enhances the Z-contrast, and EDX, this can be used to map areas and determine elemental composition. This is especially useful for samples with both heavy and light elements, and was used in Paper I to investigate the diffusion path of heavy Co and W metals into the Ti-Al-Si-N film after annealing.

5.2.2 Scanning Electron Microscopy (SEM)

In the same way as in TEM, scanning electron microscopy (SEM) utilizes an electron beam to illuminate the sample. But unlike the TEM, the beam in a SEM is focused and scanned across an area on the sample. When the beam hits the sample, the electrons in the beam interact with the sample and lose energy that is converted into heat, secondary, backscattered, and Auger electrons, light, and x-rays, among other. The image is created by displaying the various intensities for the selected signal at the position the beam was when the image was created. The resolution of a SEM is $\sim$2 nm, i.e., about an order of magnitude lower than that of a TEM. On the other hand it has a great depth of field, so it can produce images that well represents three-dimensional shapes. Also, sample preparation is in most cases not needed.

The main use of the SEM is to investigate topography of the surface of a sample, or to study the microstructure of a cross-sectional sample. The SEM can also be equipped with several different spectroscopic tools for compositional analysis. In this Thesis energy dispersive x-ray spectroscopy was used, described in detail below.

Energy Dispersive X-ray Spectroscopy (EDS)

In energy dispersive x-ray spectroscopy (EDS or EDX) x-rays emitted from the sample are detected. An EDS detector is often operated in conjunction with a SEM or TEM. The x-rays that are emitted from the sample surface are highly dependent on the electronic structure of the atoms from which they were generated, and their energy is specific for each element. This enables identification and quantification of the elements in the sample. Light elements, for example nitrogen, have low detection efficiency since the emitted x-rays have low energy and high probability of being absorbed before they reach the detector.

The accuracy can be affected by several factors, e.g., overlapping peaks of some elements, but also the homogeneity of the sample, since the probability that an x-ray escapes the sample and is detected is dependent on the energy of the x-ray and the amount and density of the material is has to escape from.

The x-rays are emitted from a large volume of the sample, of the order of 1 μm^3. In the case of thin films the substrate can influence the measurements if the penetration depth of the beam is too large.

For quantification of an element in EDS, the intensities of each element are counted in the detector at certain beam currents, and the count rates are com-

pared to standards, containing a known amount of the element of interest. X-rays show matrix effects that have to be encountered for by so-called ZAF-correction; atomic number (Z), absorption (A) and fluorescence (F). This is usually done automatically in the computer program.

5.3 Ion Beam Analysis Techniques

Ion beam analysis techniques are commonly used for compositional determination and depth profiling of a sample. Other information that can be obtained includes thickness, compositional gradients, and depth positioning of different elements. Here, Rutherford Backscattering Spectrometry (RBS) and Secondary Ion Mass Spectrometry (SIMS), both described more in detail below, were used in Paper II to determine the elemental composition of samples containing several layers.

5.3.1 Rutherford Backscattering Spectrometry (RBS)

Rutherford backscattering spectrometry (RBS) [55] is based on elastic scattering of ions, where the principle of conservation of energy and momentum during a collision applies. The sample is irradiated with an ion beam, often consisting of He^+ or H^+. The ions collide with the sample atoms and are elastically backscattered. The energies of the backscattered ions are detected, and a spectrum is obtained.

The backscattered ions with highest energy have collided with the heaviest elements in the sample, but the ion energy is also dependent on the distance travelled in the sample, meaning that ions scattered by an atom deeper in the sample has lower energy.

The measured backscattering energy spectra can be fitted to a simulation, here using the simulation program SIMNRA [56], where the fit is based on composition and thickness of the sample in order to yield an elemental depth profile.

RBS is suitable for analysis of thin films up to ∼500 nm. The films should consist of medium to heavy elements on light-element substrates. In Paper II RBS was used for determining the composition of a single layer $Hf_{0.6}Al_{0.2}Si_{0.2}N$ film that later served as a standard for SIMS depth profile analyses.

5.3.2 Secondary Ion Mass Spectrometry (SIMS)

Secondary ion mass spectrometry (SIMS) is used for surface compositional analysis by irradiating the surface of a sample with a beam of positive ions. When the sample is bombarded with ions, interactions in the top atomic layers of the sample lead to emission of various particles, including positive and negative secondary ions. The ejected ions are collected and analyzed in a mass spectrometer. Since the ions are ejected from the surface, the technique is very surface sensitive, and SIMS is capable of detecting surface impurities below 1 ppm concentration.

Different ion beams can be used, depending on the nature of the sample. Oxygen primary ions are often used for electropositive elements since the probability of generating positive secondary ions then is increased, while cesium primary ions often are used for electronegative elements.

SIMS is available in two modes; static and dynamic. Static SIMS [57] is used for sub-monolayer elemental analysis, while dynamic SIMS is used for obtaining compositional information as a function of depth below the surface. In static SIMS the aim is to obtain strong enough signals for compositional analysis, without damaging to the surface.

In dynamic SIMS [58] the beam is used to gradually sputter away the surface while recording sequentially. A plot of the intensity of a given mass signal as a function of time is given, which reflects the concentration with increasing depth. In Paper II a time-of-flight (ToF)-SIMS with two separate beams was used; one beam for etching a crater in the surface of the sample, while short pulses from the other beam was used to analyze the surface in the bottom of the crater.

5.4 Mechanical Characterization

5.4.1 Nanoindentation

Indentation techniques are the most commonly used techniques for determining the mechanical properties of a material, such as hardness and elastic modulus. In the case of thin films, special consideration has to be taken into account since what is measured is a thin film on a substantially thicker substrate. This requires a method that ensures that it is the film that is measured, without contribution from the substrate. The most common method for evaluating hardness and elastic modulus of a thin film is nanoindentation, where an indenter with a sharp diamond tip is pressed into the film. By controlling the applied load and evaluating the deformed area, hardness and elastic modulus can be determined by applying the evaluation method developed by Oliver and Pharr [59].

The hardness of a material is defined as the resistance to plastic deformation. In nanoindentation the hardness, H, is equal the applied load, P, divided by the contact area of the tip, A.

$$H = \frac{P}{A} \tag{5.4}$$

In nanoindentation, the residual indents are usually too small to be measured by optical means, so the contact area has to be calculated. For a pyramid shaped diamond Berkovich tip (that was used in all measurements in this Thesis), the contact area is given by:

$$A = 24.49 h_c^2 \tag{5.5}$$

During indentation, the applied load, P, and the indentation depth, h, is recorded continuously. The relation between the maximum indentation depth, h_{max}, the surface displacement, h_s, and the contact depth, h_c, is shown in the cross-sectional schematic illustration of an indentation in Figure 5.3. After removal of the load the material recovers elastically and the resulting indent, due to plastic deformation, have a depth, h_f.

The reduced modulus E_r is given by the equation

$$E_r = \frac{1}{2}\sqrt{\frac{\pi}{A}}\left(\frac{dP}{dh}\right), \tag{5.6}$$

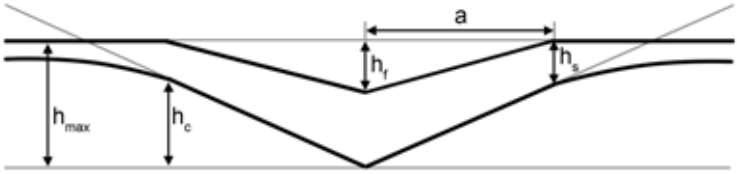

Figure 5.3. Schematic illustrition of a cross-section through an indent. Based on a figure by Oliver and Pharr [59].

where (dP/dh) is the contact stiffness that can be determined from the gradient of the first part of the unloading curve, see Figure 5.4. The elastic modulus of the sample can be calculated if Poisson's ratio (ν) is known, as well as the elastic modulus (E_i) and Poisson's ratio (ν_i) of the indenter:

$$\frac{1}{E_r} = \frac{1-\nu^2}{E} + \frac{1-\nu_i^2}{E_i}. \tag{5.7}$$

To avoid influence from substrate the penetration depth should not exceed 10 % of the film thickness. To make sure that the correct load is used, an initial test series with increasing load is performed until the maximum load is reached. The shape of the tip is crucial for correct evaluation of the acquired data. The tip wears with time, and therefore the tip contact area is calibrated with respect to a sample with known hardness and elastic modulus. Here, fused quartz has been used as reference material.

It is also important to take into account that the hardness data aquired is affected by material-dependent properties, such as microstructure, stress, grain size and grain boundaries, etc, but also on conditions during measurements such as temperature and humidity. The arc evaporated films in Paper I, have a rough surface that can influence the measurements. Therefore, they have been polished before measurements, and to avoid reduction of the film thickness, the samples were placed in tapered cross-sections.

5.4.2 Fracture Toughness

Fracture toughness is defined as the highest stress intensity that a material can withstand without fracture in the presence of a flaw. For thin films, however, traditional methods for determining toughness such as measuring the maximum stress intensity factor under plane strain conditions, does not work since the thickness usually ranges from nanometers to a few micrometers, meaning that the plane strain condition is not met [60]. For thin films, nanoindentation can be used to create cracks. The crack formation and propagation is then used as a measure of the fracture toughness.

There are mainly three different types of cracking that can occur when indenting a thin film; radial cracking, circumferential cracking and spallation, and

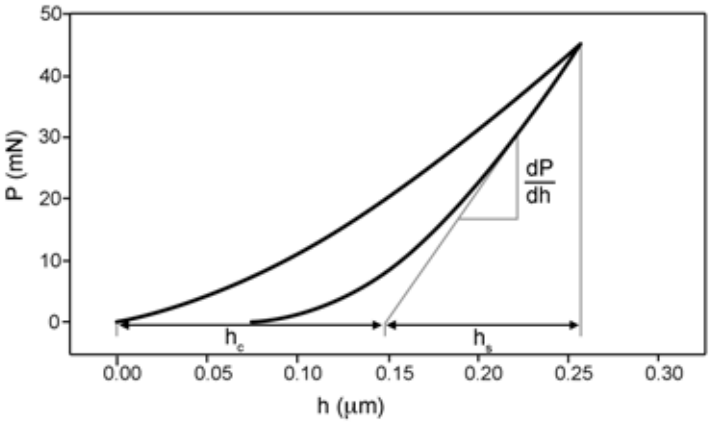

Figure 5.4. A typical nanoindentation loading-unloading curve.

channel cracking. Here, only radial cracking will be described in detail, since those cracks were the only ones present during toughness characterization in Paper II.

Radial cracks may be introduced at the surface of a ceramic material when indenting with a sharp edge indenter, e.g., a Vickers or Berkovich indenter. The relationship between the fracture toughness (K_c) and the length of the cracks (c) can be written as:

$$K_c = \alpha \left(\frac{E}{H}\right)^{1/2} \left(\frac{P}{c^{3/2}}\right), \tag{5.8}$$

in which P is the peak load at indentation, and α is an empirical constant which depends on the geometry of the indenter ($\alpha = 0.016$ for both Berkovich and Vickers type indenters). E and H are the elastic modulus and hardness of the material, respectively.

For Equation 5.8 to be valid, it is required that the indentation depth is less than 10 % of the film thickness. However, in order to produce visible cracks, there is a threshold load of 250 mN or more for most ceramic materials [61, 62], and the corresponding impressions are several micrometers in depth. Even with a shaper indenter (like the cube corner), the impressions range a few hundred nanometers in depth [63]. Thus, for thin films, it is very hard to introduce well-defined radial cracks and meet the depth limitation of nanoindentation to exclude substrate effects.

To still be able to determine fracture toughness of thin films with nanoindentation, and also to evaluate fracture toughness of films with small or no visible cracks, a fixed load was used for all indents, and only films with the same thickness grown on the same kind of substrate were evaluated. Thereby, the general trends could be studied, and the films could also be compared with reference samples measured in the same way.

CHAPTER 6

Summary of Included Papers

6.1 Paper I

In this paper, $Ti_{(1-x-y)}Al_xSi_yN_z$ thin films with $0.02 \leq x \leq 0.46$, $0.02 \leq y \leq 0.28$, and $1.08 \leq z \leq 1.29$ were grown on cemented carbide substrates in an N_2 atmosphere. $Ti_{0.75}Al_{0.25}$, $Ti_{0.75}Si_{0.25}$, and $Ti_{0.23}Al_{0.47}Si_{0.30}$ cathodes were used in an industrial scale cathodic arc evaporation system.

X-ray diffraction was used to investigate the microstructure of the as-deposited films, and it shows that the microstructure changes from nanocrystalline to x-ray amorphous by addition of 12 at% Si and 18 at% Al to TiN. HRTEM shows that the x-ray amorphous films consist of an electron-diffraction amorphous matrix with a small number of largely separated ∼2 nm crystallites of a cubic TiN-like phase.

X-ray amorphous $(Ti_{0.26}Al_{0.46}Si_{0.28})N_{1.17}$ films were post-deposition annealed in an Ar atmosphere for 2 h at temperatures between 500 °C and 1100 °C. Room temperature *ex-situ* x-ray diffraction showed no change in microstructure up to 800 °C. At 900 °C nanocrystals start to form in the films, which was confirmed by HRTEM imaging. The crystallization occurs by coarsening of nanocrystallites, preferentially in Ti-rich layers induced by substrate rotation. At 1100 °C severe out-diffusion of Co and W from the substrate occurs, and the films recrystallize into c-TiN and w-AlN, which was evidenced by a combination of XRD, STEM/HAADF imaging, and EDX elemental mapping. ∼1.5 μm of the film thickness has recrystallized at 1100 °C, with a growth front advancing from the substrate into an otherwise homogeneous film.

Nanoindentation experiments show that the films exhibit age hardening up to 1000 °C with more than a 40% increase in hardness from 21.9 GPa for as-deposited films to 31.6 GPa at 1000 °C.

6.2 Paper II

The second paper reports on both single layer $Hf_{1-x-y}Al_xSi_yN$ ($0 \leq x \leq 0.2$ and $0 \leq y \leq 0.2$) and multilayer a-$Hf_{0.6}Al_{0.2}Si_{0.2}N$/nc-HfN films grown on Si(001) substrates using a single $Hf_{0.60}Al_{0.20}Si_{0.20}$ alloy target in an 5%-N_2/Ar atmosphere.

By using a magnetically-unbalanced reactive magnetron sputtering system it was possible to control both composition and nanostructure of the films during growth by independently varying the ion energy (E_i) and the ion-to-metal flux ratio (J_i/J_{Me}) incident at the film surface.

HRTEM imaging showed that with $J_i/J_{Me} = 8$, the composition and nanostructure of the films ranges from x-ray amorphous with a Hf content of 0.6 at $E_i = 15$ eV, to an amorphous matrix with encapsulated nanocrystals when the Hf content is between 0.66 and 0.84 at $E_i = 25$-35 eV, to nanocrystalline with a Hf content between 0.96 and 1.00 at $E_i = 45$-65 eV. Varying J_i/J_{Me} with constant $E_i = 13$ eV yields electron-diffraction amorphous films at $T_s = 100$ °C.

The multilayer films, a-$Hf_{0.6}Al_{0.6}Si_{0.6}N$/nc-HfN, with periods $\Lambda = 2$-20 nm were produced by changing the E_i end switching periods. Nanoindentation experiments show that the multilayer films exhibit enhanced fracture toughness compared to polycrystalline VN, TiN, and $Ti_{0.5}Al_{0.5}N$ reference samples. The multilayer hardness values increase monotonically from 20 GPa with $\Lambda = 20$ nm to 27 GPa with $\Lambda = 2$ nm.

CHAPTER 7

Future Work and Outlook

The foundation for all research carried out in the Thin Film Physics Division, is the understanding of the relationship between *synthesis, properties, structure and composition,* and *modeling*. My work this far has included the first three of these cornerstones.

In this work I have shown that it is possible to distort the crystallinity in transition metal nitride films and reach beyond x-ray amorphousness. I have shown that we are on the right track for achieving fully electron-diffraction amorphous films, both by industrial scale cathodic arc evaporation and laboratory scale magnetron sputtering equipment. I have studied how the microstructure evolves depending on composition and deposition parameters, and I have characterized different properties of the amorphous films.

From here on there are several possible paths to follow during the remainder of my graduate studies, and I will discuss some of them briefly here, together with some of the challenges I anticipate we are to face on the way.

Synthesis

To further distort the crystallinity in the arc evaporated films that we reported on in Paper I, addition of more Si is needed. This far, we have been limited by the available cathodes. I am convinced that we can achieve electron-diffraction amorphous films in the Ti-Si-N system, with or without additional Al, if we can increase the Si content in the cathodes to at least 30 at%.

An alternative route could be to add other elements to the system. Here, B is interesting, since it has been reported earlier that B can distort the crystallinity in TiN [64–67]. Zr is also an appealing alternative, either as addition, or as replacement for Ti. ZrN has been reported to be amorphous for nitrogen overstoichiometry [68]. In general, an increased complexity of the materials system by

adding more components that are known to have large size differences and bond coordination would be favorable. Here the high entropy alloy systems could be interesting archetypes.

For the Hf-Al-Si-N films reported on in Paper II, there are two main areas to work with regarding synthesis. Either, the Si content is increased in the target, or the substrate temperature has to be lowered. The later would call for a redesign of the deposition system, since the water cooling available today does not provide low enough temperatures.

Characterization

The characterization includes both *structure and composition* as well as *properties*. Working with amorphous films inevitably leads to problems with seeing what you have. Some techniques, like XRD, are insensitive to crystallites smaller than a few nm. But also TEM, that was used in both Paper I and Paper II to examine the microstructure of the films, has its limitations. Even HRTEM has problems to detect crystallites smaller than $\sim$1 nm. We simply cannot see the microstructure any more! Establishing lack of crystallinity in films in the TEM is not straight-forward. The thickness of the sample, even though thinned to electron transparency, greatly exceeds the size of the crystallites we are trying to see, and what appear to be an amorphous matrix, or even a fully amorphous films, might actually be nanograins oriented in different directions. Also, recrystallization of the sample under illumination of the beam is a risk.

As the size of what we want to detect decreases steadily, we need better and more advanced tools for characterization. Luckily there is a steadily ongoing development of instruments and methods. During the continuation of my graduate studies I would thus very much like to take the opportunity to deepen my knowledge about the systems I already master, but also explore new techniques to widen my knowledge.

Bibliography

[1] *Modern Metal Cutting - A Practical Handbook*. AB Sandvik Coromant, 1994.

[2] S.M. Kosslyn. Through the glass lightly. *Science*, 267:1615, 1995.

[3] J. P. Chu, J.S.C. Jang, J.C. Huang, H.S. Chou, Y. Yang, J.C. Ye, Y.C. Wang, J.W. Lee, F.X. Liu, P.K. Liaw, Y.C. Chen, C.M. Lee, C.L. Li, and C. Rullyani. Thin film metallic glasses: Unique properties and potential applications. *Thin Solid Films*, 520(16):5097 – 5122, 2012.

[4] M. Magnusson, M. Andersson, J. Lu, L. Hultman, and U. Jansson. Electronic structure and chemical bonding of amorphous chromium carbide thin films. *Journal of Physics: Condensed Matter*, 24:225004, 2012.

[5] K. Kádas, M. Andersson, E. Holmström, H. Wende, O. Karis, S. Urbonaite, S. M. Butorin, S. Nikitenko, K. O. Kvashnina, U. Jansson, and O. Eriksson. Structural properties of amorphous metal carbides: Theory and experiment. *Acta Materialia*, 60:4720–4728, 2012.

[6] M. Andersson, S. Urbonaite, E. Lewin, and U. Jansson. Magnetron sputtering of Zr–Si–C thin films. *Thin Solid Films*, 520(20):6375 – 6381, 2012.

[7] X. Sun, J. S. Reid, E. Kolawa, M.-A. Nicolet, and R. P. Ruiz. Reactively sputtered Ti-Si-N films. II. Diffusion barriers for Al and Cu metallizations on Si. *Journal of Applied Physics*, 81(2):664–671, 1997.

[8] J.-T. No, J.-H. O, and C. Lee. Evaluation of Ti-Si-N as a diffusion barrier between copper and silicon. *Materials Chemistry and Physics*, 63(1):44 – 49, 2000.

[9] Y. Wang, C. Zhu, Z. Song, and Y. Li. High temperature stability of Zr–Si–N diffusion barrier in Cu/Si contact system. *Microelectronic Engineering*, 71(1):69 – 75, 2004.

[10] M.-A. Nicolet. Ternary amorphous metallic thin films as diffusion barriers for Cu metallization. *Applied Surface Science*, 91(1–4):269 – 276, 1995.

[11] J.S. Reid, E. Kolawa, R.P. Ruiz, and M.-A. Nicolet. Evaluation of amorphous (Mo, Ta, W)-Si-N diffusion barriers for Si-Cu metallizations. *Thin Solid Films*, 236(1-2):319 – 324, 1993.

[12] Y.-J. Lee, B.-S. Suh, S.-K. Rha, and C.-O. Park. Structural and chemical stability of Ta–Si–N thin film between Si and Cu. *Thin Solid Films*, 320(1):141 – 146, 1998.

[13] C. Lee and Y.-H. Shin. Ta-Si-N as a diffusion barrier between Cu and Si. *Materials Chemistry and Physics*, 57(1):17 – 22, 1998.

[14] J. Musil, R. Daniel, P. Zeman, and O. Takai. Structure and properties of magnetron sputtered Zr–Si–N films with a high ($\geq$25 at%) Si content. *Thin Solid Films*, 478(1-2):238 – 247, 2005.

[15] R. Daniel, J. Musil, P. Zeman, and C. Mitterer. Thermal stability of magnetron sputtered Zr–Si–N films. *Surface and Coatings Technology*, 201(6):3368 – 3376, 2006.

[16] M. Ohring. *The Materials Science of Thin Films*. Academic Press, 1992.

[17] F. M. Penning. Die Glimmentladung bei niedrigem Druck zwischen koaxialen Zylindern in einem axialen Magnetfeld. *Physica*, 3(9):873–894, 1936.

[18] E. Kay. Magnetic field effects on an abnormal truncated glow discharge and their relation to sputtered thin-film growth. *Journal of Applied Physics*, 34(4):760–768, 1963.

[19] W.D. Gill and E. Kay. Efficient low pressure sputtering in a large inverted magnetron suitable for film synthesis. *The Review of Scientific Instruments*, 36(3):277–282, 1965.

[20] R. K. Waits. *Planar Magnetron Sputtering*. In Thin Film Processes, edited by J. L. Vossen and W. Kern. Academic Press, 1978.

[21] I. Petrov, F. Adibi, J.E. Greene, W.D. Sproul, and W.-D. Münz. Use of an externally applied axial magnetic field to control ion/neutral flux ratios incident at the substrate during magnetron sputter deposition. *Journal of Vacuum Science & Technology A*, 10(5):3283–3287, 1992.

[22] J.E. Greene, S.A. Barnett, J.-E. Sundgren, and A. Rockett. *Low-energy Ion/Surface Interactions During Film Growth From the Vapor Phase*. In Ion Beam Assisted Film Growth, edited by T. Itoh. Elsevier Science Publisher, 1989.

[23] S. Berg and I. Katardjiev. Resputtering effects during ion beam assisted deposition and the sputter yield amplification effect. *Surface and Coatings Technology*, 84(1–3):353 – 362, 1996.

[24] J. L. Vossen and J.J. Cuomo. *Glow Discharge Sputter Deposition*. Thin Film Processes, edited by J. L. Vossen and W. Kern. Academic Press, 1978.

[25] O. Almén and G. Bruce. Collection and sputtering experiments with noble gas ions. *Nuclear Instruments and Methods*, 11:257–278, 1961.

[26] O. Almén and G. Bruce. Sputtering experiments in the high energy region. *Nuclear Instruments and Methods*, 11:279–289, 1961.

[27] N. Laegreid and G. K. Wehner. Sputtering yields of metals for Ar^+ and Ne^+ ions with energies from 50 to 600 ev. *Journal of Applied Physics*, 32(3):365–369, 1961.

[28] A. H. Eltoukhy and J. E. Greene. Diffusion enhancement due to low-energy ion bombardment during sputter etching and deposition. *Journal of Applied Physics*, 51(8):4444–4452, 1980.

[29] R. Behrisch. *Sputtering by particle bombardment: I. Physical sputtering of single-element solids*. Springer-Verlag, Berlin, 1981.

[30] A. Anders. Ion charge state distributions of vacuum arc plasmas: The origin of species. *Physical Review E*, 55:969–981, 1997.

[31] A. Anders. Approaches to rid cathodic arc plasmas of macro- and nanoparticles: a review. *Surface and Coatings Technology*, 120-121:319–330, 1999.

[32] R. L. Boxman, D. M. Sanders, P. J. Martin, and J. M. Laferty. *Handbook of Vacuum Arc Science, Fundamentals and Applications*. Noyes Publications, New Jersey, 1995.

[33] A. Eriksson, J.Q. Zhu, N. Ghafoor, M.P. Johansson, J. Sjölén, J. Jensen, M. Odén, L. Hultman, and J. Rosén. Ti-Si-C-N thin films grown by reactive arc evaporation from Ti_3SiC_2 cathodes. *Journal of Materials Research*, 26:874–881, 2011.

[34] B. A. Movchan and A. V. Demchishin. Study of the structure and properties of thick vacuum condensates of nickel, titanium, tungsten, aluminium oxide and zirconium dioxide. *Physics of Metals and Metallography*, 28:83–90, 1969.

[35] J. A. Thornton. Influence of apparatus geometry and deposition conditions on the structure and topography of thick sputtered coatings. *Journal of Vacuum Science and Technology*, 11:666, 1974.

[36] A. Anders. A structure zone diagram including plasma-based deposition and ion etching. *Thin Solid Films*, 518(15):4087–4090, 2010.

[37] C. Kittel. *Introduction to Solid State Physics 8^{th} edition*. John Wiley & Sons, Inc., 2005.

[38] R. Zallen. *The Physics of Amorphous Solids*. John Wiley & Sons, Inc., 1983.

[39] C. Michaelsen, C. Gente, and R. Bormann. The thermodynamics of amorphous phases in immiscible systems: The example of sputter-deposited Nb–Cu alloys. *Journal of Applied Physics*, 81(9):6024–6030, 1997.

[40] H. Hecht, G. Weigang, S. Eickert, and U. Geyer. Formation area of thin amorphous Zr-Mn and Zr-Ta films prepared by cocondensation. *Zeitschrift für Physik B*, 1996.

[41] J. C. Slater. Atomic radii in crystals. *The Journal of Chemical Physics*, 41(10):3199–3204, 1964.

[42] L. E. Toth. *Transition Metal Carbides and Nitrides*. Academic Press, 1971.

[43] P. H. Mayrhofer, C. Mitterer, and H. Clemens. Self-organized nanostructures in hard ceramic coatings. *Advanced Engineering Materials*, 7:1071–1082, 2005.

[44] M. W. Barsoum. *Fundamentals of Ceramics*. Taylor & Francis Group, NY., 2003.

[45] B. M. Howe. *Growth, physical properties, and nanostructuring of epitaxial metastable Hafnium Aluminum Nitride*. PhD thesis, University of Illinois at Urbana-Champaign, 2010.

[46] Synthesis of metastable epitaxial zinc-blende structure AlN by solid-state reaction. I. petrov and e. mojab and r. c. powell and j. e. greene and l. hultman and j.-e. sundgren. *Applied Physics Letters*, 60(20):2491, 1992.

[47] F. Adibi, I. Petrov, L. Hultman, U. Wahlstrom, T. Shimizu, D. McIntyre, J. E. Greene, and J.-E. Sundgren. Defect structure and phase transitions in epitaxial metastable cubic $Ti_{0.5}Al_{0.5}N$ alloys grown on MgO(001) by ultra-high-vacuum magnetron sputter deposition. *Journal of Applied Physics*, 69(9):6437–6450, 1991.

[48] I. Tomaszkiewicz. Thermodynamics of silicon nitride. Standard molar enthalpy of formation of amorphous Si_3N_4 at 298.15 K. *Journal of Thermal Analysis and Calorimetry*, 65(2):425–433, 2001.

[49] A. Zerr, G. Miehe, G. Serghiou, E. Kroke, R. Riedel, H. Fuesz, P. Kroll, and R. Boehler. Synthesis of cubic silicon nitride. *Nature*, 400(6742):340, 1999.

[50] D. A. Porter and K. E. Easterling. *Phase Transformations in Metals and Alloys 2nd Edition*. Taylor & Francis Group, NY., 2004.

[51] R. A. L. Jones. *Soft Condensed Matter*. Oxford University Press, 2002.

[52] A. Hörling, L. Hultman, M. Odén, J. Sjölén, and L. Karlsson. Mechanical properties and machining performance of $Ti_{1-x}Al_xN$-coated cutting tools. *Surface and Coatings Technology*, 191:384–392, 2005.

[53] R. Erni, M. D. Rossell, C. Kisielowski, and U. Dahmen. Atomic-resolution imaging with a sub-50-pm electron probe. *Physical Review Letters*, 102:096101–096104, 2009.

[54] D. B. Williams and C. B. Carter. *Transmission Electron Microscopy*. Springer Science, 2009.

[55] L. Palmetshofer. *Rutherford Back-scattering Spectroscopy (RBS)*. Surface and Thin Film Analysis: Principles, Instrumentation, Applications, edited by H. Bubert and H. Jenett. Wiley-VCH Verlag GmbH, 2002.

[56] M. Mayer. SIMNRA, a simulation program for the analysis of NRA, RBS and ERDA. *American Institute of Physics Conference Proceedings*, 475:541, 1999.

[57] H. F. Arlinghaus. *Static Secondary Ion Mass Spectrometry (SSIMS)*. Surface and Thin Film Analysis: Principles, Instrumentation, Applications, edited by H. Bubert and H. Jenett. Wiley-VCH Verlag GmbH, 2002.

[58] H. Hutter. *Dynamic Secondary Ion Mass Spectrometry*. Surface and Thin Film Analysis: Principles, Instrumentation, Applications, edited by H. Bubert and H. Jenett. Wiley-VCH Verlag GmbH, 2002.

[59] W. C. Oliver and G. M. Pharr. An improved technique for determining hardness and elastic modulus using load and displacement sensing indentation experiments. *Journal of Materials Research*, 7:1564–83, 1992.

[60] S. Zhang and X. Zhang. Toughness evaluation of hard coatings and thin films. *Thin Solid Films*, 520(7):2375 – 2389, 2012.

[61] G.M. Pharr. Measurement of mechanical properties by ultra-low load indentation. *Materials Science and Engineering: A*, 253(1–2):151 – 159, 1998.

[62] J. Lankford and D. L. Davidson. Indentation plasticity and microfracture in silicon carbide. *Journal of Materials Science*, 14:1669–1675, 1979.

[63] X. Li, D. Diao, and B. Bhushan. Fracture mechanisms of thin amorphous carbon films in nanoindentation. *Acta Materialia*, 45(11):4453 – 4461, 1997.

[64] L. Chaleix and J. Machet. Study of the composition and of the mechanical properties of TiBN films obtained by D.C. magnetron sputtering. *Surface and Coatings Technology*, 91(1–2):74 – 82, 1997.

[65] P.H. Mayrhofer, H. Willmann, and C. Mitterer. Recrystallization and grain growth of nanocomposite Ti–B–N coatings. *Thin Solid Films*, 440(1–2):174 – 179, 2003.

[66] Y.H. Lu, Z.-J. Liu, and Y.G. Shen. Investigation of nanostructure evolution and twinning of nanocrystallites in Ti–B_x–N_y nanocomposite thin films deposited by magnetron sputtering at low temperature by means of HRTEM and Monte Carlo simulations. *Acta Materialia*, 54(11):2897 – 2905, 2006.

[67] J. Neidhardt, M. O'Sullivan, A.E. Reiter, W. Rechberger, W. Grogger, and C. Mitterer. Structure–property–performance relations of high-rate reactive arc-evaporated Ti–B–N nanocomposite coatings. *Surface and Coatings Technology*, 201(6):2553 – 2559, 2006.

[68] H.M Benia, M Guemmaz, G Schmerber, A Mosser, and J.-C Parlebas. Investigations on non-stoichiometric zirconium nitrides. *Applied Surface Science*, 200(1–4):231 – 238, 2002.